Rapid Dynamical Evolution of ITCZ Events over the East Pacific

ALEX O. GONZALEZ,[a] INDRANI GANGULY,[a] MARIE C. MCGRAW,[b] AND JAMES G. LARSON[c]

[a] *Department of Geological and Atmospheric Sciences, Iowa State University, Ames, Iowa*
[b] *Department of Atmospheric Sciences, University of Washington, Seattle, Washington*
[c] *Department of Aerospace Engineering, Iowa State University, Ames, Iowa*

(Manuscript received 17 March 2021, in final form 10 October 2021)

ABSTRACT: The latitudinal location of the east Pacific Ocean intertropical convergence zone (ITCZ) changes on time scales of days to weeks during boreal spring. This study focuses on tropical near-surface dynamics in the days leading up to the two most frequent types of ITCZ events, nITCZ (Northern Hemisphere) and dITCZ (double). There is a rapid daily evolution of dynamical features on top of a slower, weekly evolution that occurs leading up to and after nITCZ and dITCZ events. Zonally elongated bands of anomalous cross-equatorial flow and off-equatorial convergence rapidly intensify and peak 1 day before or the day of these ITCZ events, followed 1 or 2 days later by a peak in near-equatorial zonal wind anomalies. In addition, there is a wide region north of the southeast Pacific subtropical high where anomalous northwesterlies strengthen prior to nITCZ events and southeasterlies strengthen before dITCZ events. Anomalous zonal and meridional near-surface momentum budgets reveal that the terms associated with Ekman balance are of first-order importance preceding nITCZ events, but that the meridional momentum advective terms are just as important before dITCZ events. Variations in cross-equatorial flow are promoted by the meridional pressure gradient force (PGF) prior to nITCZ events and the meridional advection of meridional momentum in addition to the meridional PGF before dITCZ events. Meanwhile, variations in near-equatorial easterlies are driven by the zonal PGF and the Coriolis force preceding nITCZ events and the zonal PGF, the Coriolis force, and the meridional advection of zonal momentum before dITCZ events.

KEYWORDS: Intertropical convergence zone; Dynamics; Momentum; Nonlinear dynamics; Synoptic climatology

1. Introduction

The intertropical convergence zone (ITCZ) is a zonal band of convection that wraps around Earth and produces the majority of Earth's rainfall. There are still longstanding climate model ITCZ biases (e.g., Mechoso et al. 1995; Lin 2007; Bellucci et al. 2010; Zhang et al. 2015; Tian and Dong 2020), especially in the southern east Pacific Ocean from December through May (Adam et al. 2018; Woelfle et al. 2019; Song and Zhang 2019). These months also coincide with the most rapid variations in the latitudinal position of the east Pacific ITCZ in infrared satellite imagery, taking on any of five ITCZ states: Northern Hemisphere (nITCZ), Southern Hemisphere (sITCZ), double (dITCZ), equatorial (eITCZ), or absent (aITCZ) (Henke et al. 2012; Haffke et al. 2016). An example of such high-frequency variations in ITCZ state is shown in Fig. S1 in the online supplemental material for 6–18 March 2018.

Even though recent advances in explaining ITCZ shifts on seasonal and longer time scales have been made, highlighted by the atmosphere–ocean hemispheric energy balance framework [see reviews by Schneider et al. (2014), Kang et al. (2018), and Hill (2019)], the processes that drive the time evolution of subseasonal and shorter-time-scale ITCZ shifts are still largely unknown. Haffke et al. (2016) show evidence of significant roles for processes at multiple time scales for nITCZs, dITCZs, and sITCZs, including the large-scale dynamics, near-surface moist thermodynamics, and radiation (Haffke et al. 2016; Yang and Magnusdottir 2016). However, they emphasize the need to better understand the large-scale atmospheric dynamics for the two most common boreal spring ITCZ states, nITCZ and dITCZ.

To understand the dynamics near the ITCZ, many studies focus on monthly or longer time scales and employ steady-state balances of the ITCZ boundary layer. For example, some studies use a balance between surface drag, the Coriolis force, and the pressure gradient force (e.g., Lindzen and Nigam 1987). This is otherwise known as classical Ekman balance (Ekman 1905). Other studies have shown more accurate representations of tropical circulations using the linear mixed layer model of Stevens et al. (2002), which is an extension of Ekman balance with the addition of horizontal momentum exchange between the boundary layer and the free troposphere and a linearization of surface drag (e.g., McGauley et al. 2004; Back and Bretherton 2009; Duffy et al. 2020). When considering applying these theories to subseasonal or shorter-time-scale ITCZs, where transient dynamics play an important role, a more general theory that includes the horizontal advection of the horizontal momentum may be more appropriate (Mahrt 1972; Holton 1975; Tomas et al. 1999; Sobel and Neelin 2006; Schneider and Bordoni 2008; Gonzalez et al. 2016; Gonzalez and Schubert 2019).

Denotes content that is immediately available upon publication as open access.

Supplemental information related to this paper is available at the Journals Online website: https://doi.org/10.1175/jcli-d-21-0216.s1.

Corresponding author: Alex O. Gonzalez, agon@iastate.edu

DOI: 10.1175/JCLI-D-21-0216.1

Gonzalez et al. (2016) and Gonzalez and Schubert (2019) illustrate that when the boundary layer meridional flow is strong enough, as it often is in the east Pacific, the meridional advection of the meridional momentum acts to sharpen regions of meridional convergence and broaden regions of meridional divergence; this behavior can be attributed to the embedded Burgers' equation (Burgers 1948) in the meridional momentum equation (Holton 1975; Gonzalez et al. 2016). Furthermore, through the meridional advection of zonal momentum, meridional gradients of the zonal wind become more concentrated in the same regions where convergence becomes narrower. This creates distinct zonally elongated zones of collocated low-level convergence and cyclonic relative vorticity (Gonzalez et al. 2016; Gonzalez and Schubert 2019). In this way, narrow ITCZs tend to occur where there is strong cross-equatorial low-level flow (e.g., east Pacific and Atlantic Oceans).

In this paper, we investigate the observed time evolution of the near-surface, large-scale dynamics in high-resolution data in the days leading up to the two most frequent February–April east Pacific ITCZ states, nITCZ and dITCZ, to improve our understanding of ITCZ shifts on subseasonal and shorter time scales. We compute anomalous zonal and meridional surface momentum budgets leading up to these events, with an eye on better understanding the roles of meridional momentum advection and the terms associated with classical Ekman balance. We focus on the near-surface dynamics because they are closely tied to air–sea fluxes, moist thermodynamics, and low-level ITCZ convergence, for which there are existing theories of the low-level horizontal momentum budgets (e.g., Lindzen and Nigam 1987; Tomas et al. 1999; Back and Bretherton 2009; Gonzalez et al. 2016).

The paper is organized as follows. Section 2 describes the remotely sensed observations and reanalysis datasets used as well as how we determine submonthly ITCZ events from the 3-hourly ITCZ states in Haffke et al. (2016). We also present the horizontal surface momentum budget equations. Section 3 has four subsections, with the first motivating the investigation of the large-scale surface dynamics associated with the east Pacific ITCZ. In the last three subsections of section 3, we illustrate the time evolution of composites of the large-scale surface dynamics for ITCZ events, and we scrutinize the surface zonal and meridional momentum budgets. Section 4 summarizes our results and discusses future directions to better understand February–April east Pacific ITCZ events.

2. Data and methods

a. Observational and reanalysis datasets

Daily 0.25°-resolution ocean surface (10 m) winds are estimated using the National Aeronautics and Space Administration (NASA) Quick Scatterometer (QuikSCAT) dataset for the time period of August 1999–July 2009 (SeaPAC 2006). Due to rain contamination, 50%–60% of ocean winds measurements are acceptable over the tropical east Pacific during January–May, and therefore daily averaged or single-valued QuikSCAT winds are used in place of twice-daily winds. Daily accumulated 0.25°-resolution precipitation rates are from the Tropical Rainfall Measuring Mission (TRMM) Multisatellite Precipitation Analysis (TMPA) dataset for 1998–2012 (Huffman and Bolvin 2015). All other variables, including 10-m horizontal winds, 10-m horizontal divergence, 2-m temperature, 2-m specific humidity, and mean sea level pressure, are from the most recent European Centre for Medium-Range Weather Forecasts (ECMWF) reanalysis (ERA5) for 1980–2012 (Hersbach et al. 2020). The ERA5 data are daily averaged at 0.25° resolution. Anomalies for all variables are computed by removing a climatological annual cycle that is smoothed using the first four harmonics of the raw annual cycle.

For Figs. 5–8, statistical significance at the $\alpha = 0.1$ level is assessed at each grid point by using the field significance test of Wilks (2016), which accounts for spatial autocorrelation by controlling the false discovery rate. The method computes the cosine of latitude weighted p value for all grid points, sorts them, and sets a new threshold p value based on the distribution of p values.

b. Submonthly ITCZ events

Submonthly ITCZ "events" are determined from a 3-hourly ITCZ state dataset described in Haffke et al. (2016) for January–May 1980–2012. A pattern recognition algorithm (Henke et al. 2012) produces 3-hourly ITCZ states by analyzing 33 years of GridSat satellite data (Knapp et al. 2011) over 20°S–20°N, 90°W –180°. The five ITCZ states that were identified using the ITCZ detection algorithm of Henke et al. (2012) are the Northern Hemisphere ITCZ (nITCZ), Southern Hemisphere ITCZ (sITCZ), double ITCZ (dITCZ), equatorial ITCZ (eITCZ), and absent ITCZ (aITCZ). Zonally elongated ITCZs are detected in all states except aITCZ, which accounts for weak or localized convection. Three-hourly ITCZ states are used to produce daily ITCZ states, where a daily ITCZ state is only assigned when one ITCZ state occurs for at least 6 out of 8 (6/8) 3-hourly time stamps. Our results are insensitive to the choices of 5/8 to 8/8 three-hourly time stamp thresholds. Note that daily ITCZ states are assigned for 93% of all days in the January–May 1980–2012 time period using the chosen 6/8 threshold; the remaining 7% of days are not assigned a daily ITCZ state. Note that the absent ITCZ state differs from the times that are not assigned a state in that absent ITCZ is determined explicitly by the pattern recognition algorithm. From the five daily ITCZ states (dITCZ, nITCZ, sITCZ, aITCZ, and eITCZ), submonthly ITCZ events are defined as daily ITCZ states that persist between at least 2 and 30 days, aimed to capture submonthly variability and reduce noise originating from 3-hourly states produced by the ITCZ state algorithm.

Figure 1 shows the January–May 1980–2012 temporal variability of submonthly ITCZ events as well as the percentage distribution of each of the five types of ITCZ events for the main season of interest in this study, February–April. The resulting percentages are similar to the March–April daily ITCZ states from Haffke et al. (2016), with nITCZ (41%) and dITCZ (30%) events being most dominant compared to 39%

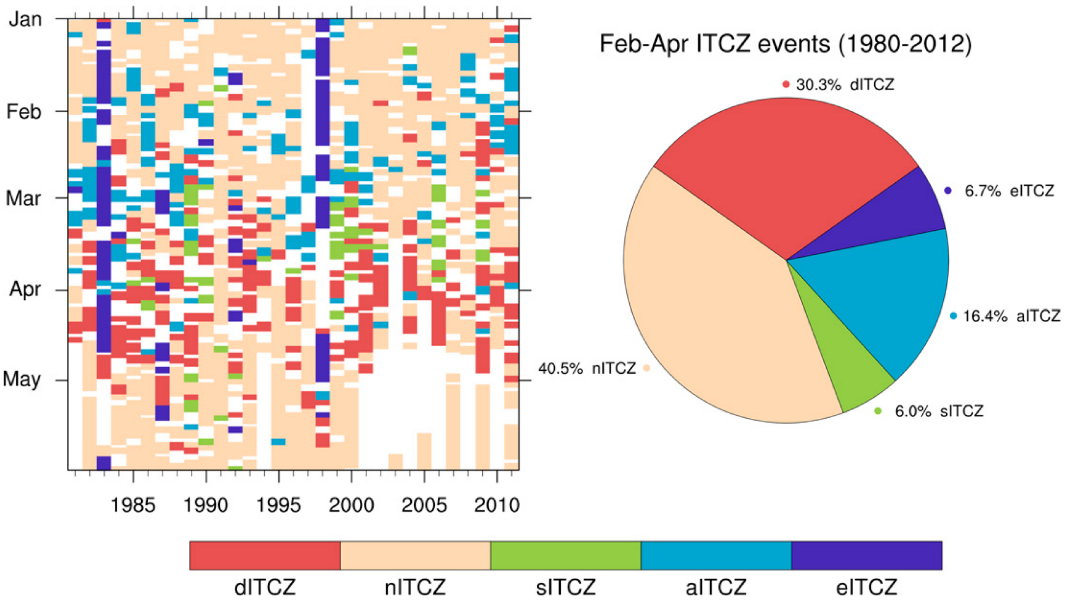

FIG. 1. (left) Temporal distribution of submonthly ITCZ events for January–May 1980–2012 based on 3-hourly GridSat satellite imagery ITCZ states (Henke et al. 2012; Haffke et al. 2016). (right) Percentage distribution of ITCZ events for the months of focus for this paper, February–April during 1980–2012.

and 34%, respectively, in Haffke et al. (2016). The third most dominant type of ITCZ events is aITCZ events (16.4%), while sITCZ (6.0%) and eITCZ (6.7%) events occur least often and have been suggested to be linked to El Niño–Southern Oscillation (Haffke et al. 2016; Yang and Magnusdottir 2016).

c. *Anomalous horizontal surface momentum budgets*

The anomalous surface zonal and meridional momentum budget equations are given by

$$\frac{\partial u}{\partial t} = -u\frac{\partial u}{\partial x} - v\frac{\partial u}{\partial y} - R_d T_v \frac{\partial \ln p}{\partial x} + f_e v + P_u + K_u, \qquad (1)$$

$$\frac{\partial v}{\partial t} = -u\frac{\partial v}{\partial x} - v\frac{\partial v}{\partial y} - R_d T_v \frac{\partial \ln p}{\partial y} - f_e u + P_v + K_v. \qquad (2)$$

Each of the seven terms in these equations is computed with total (climatology + anomaly) individual fields and their smoothed climatology is removed after multiplication of covarying terms. For example, $v(\partial v/\partial y)$ stands for $[v_{\text{total}}(\partial v/\partial y)_{\text{total}}]'$, where $(\cdot)_{\text{total}}$ and $(\cdot)'$ are total and anomalous fields, respectively. In Eqs. (1) and (2), u and v are the 10-m zonal and meridional velocities, respectively, p is mean sea level pressure, $T_v = T[1 + (R_v/R_d - 1)q]$ is 2-m virtual temperature, T is 2-m temperature, q is 2-m specific humidity, R_v and R_d are the water vapor and dry gas constants, respectively, t is time, $\delta x = a\cos\phi\delta\lambda$ and $\delta y = a\delta\phi$ are the zonal and meridional distances, respectively, a is Earth's radius, ϕ is latitude in radians, $f_e = (2\Omega\sin\phi + u\tan\phi/a)$ is the effective Coriolis parameter (Coriolis parameter plus the metric term), and Ω is Earth's rotation rate. The zonal and meridional accelerations due to parameterized physical processes (surface drag, convective momentum transport, etc.) are given by P_u and P_v, respectively. They are taken at the model level closest to the surface. The terms K_u and K_v are the residuals of the zonal and meridional momentum budget, respectively, and mainly represent horizontal diffusion terms, which are the only terms not explicitly provided by ERA5. Note that all derivatives are computed via centered finite differences and the $u(\partial u/\partial x)$ and $v(\partial v/\partial x)$ terms are computed as $\partial(u^2/2)/\partial x$ and $\partial(v^2/2)/\partial y$. Because specific humidity at 2 m is not provided by ERA5, it is postprocessed and calculated using the 2-m dewpoint temperature and mean sea level pressure. Note that we focus on the surface momentum budgets rather than boundary layer–averaged budgets primarily to most accurately diagnose the pressure gradient force. If pressure level data were used, the estimate of the pressure gradient force could contain residuals associated with the change in vertical coordinate system (from hybrid levels).

3. Results

a. *Seasonal and regional ITCZ and low-level dynamics*

We provide supporting evidence of the robust relationship between ITCZ precipitation and near-ITCZ low-level atmospheric dynamics over the east Pacific Ocean by examining their seasonal and regional variability. In Fig. 2, we show trimonthly averaged (February–April, May–July, August–October, and November–January) plots of the TMPA precipitation rate and QuikSCAT surface winds and divergence only over the oceans. There is generally a positive correlation

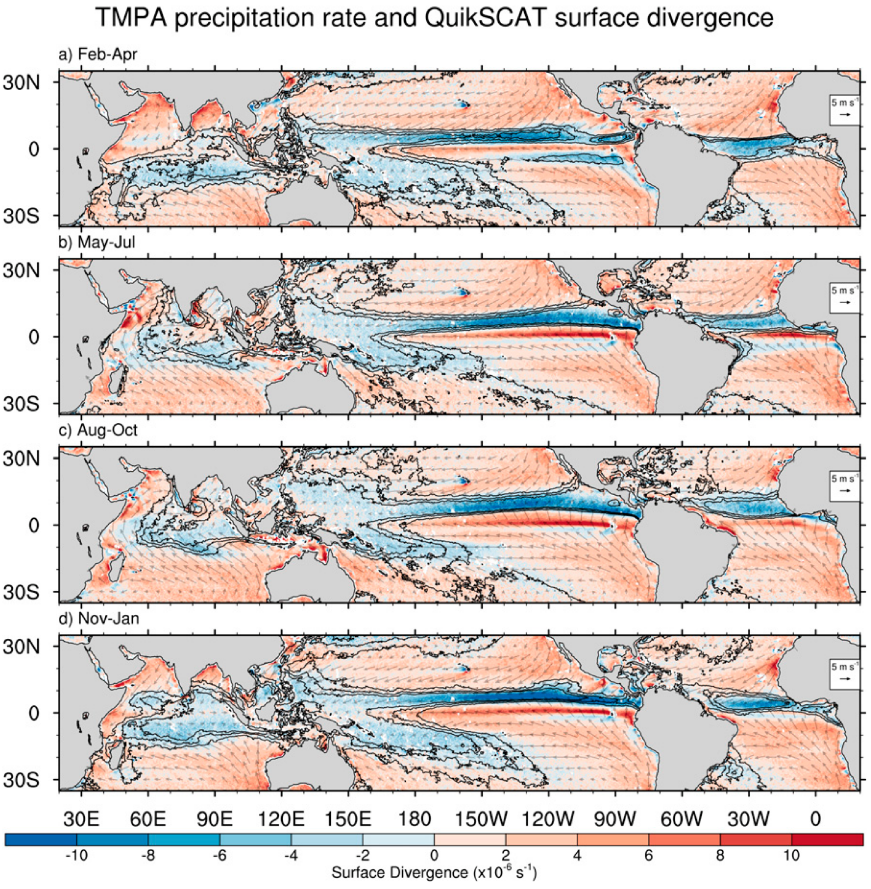

FIG. 2. Trimonthly averaged QuikSCAT horizontal surface winds (vectors), divergence (shading), and TMPA precipitation rate (contour lines every 1 mm day^{-1}, from 3 to 7 mm day^{-1}) for (a) February–April during 2000–09, (b) May–July during 2000–09, (c) August–October during 1999–2008, and (d) November–January during 1999–2008.

between surface wind convergence and tropical precipitation rate, with regions of surface convergence collocated with regions of high precipitation rates. At the same time, there are regions with stronger correlations than others, such as the ITCZ east of the date line in the Pacific Ocean and the ITCZ in the Atlantic Ocean. Figure 2 reaffirms the notion that there is a second zonally elongated convergence zone over the east Pacific year-round even though that convergence zone is not always coupled to precipitation (Liu and Xie 2002). The east Atlantic also has a second zonally elongated convergence zone not tied to precipitation during the months of November–January and May–July.

To quantify the seasonally and regionally dependent relationship between ITCZ precipitation rate and surface wind convergence, Fig. 3 shows the monthly variation of the pattern correlation between TMPA precipitation and QuikSCAT surface wind convergence for five oceanic regions: 1) the global tropics (15°S–15°N, all longitudes), 2) the eastern Pacific Ocean (15°S–15°N, 90°–150°W), 3) the western Pacific Ocean (15°S–15°N, 150°E–150°W), 4) the Atlantic Ocean (15°S–15°N, 0°–50°W), and 5) the Indian Ocean (15°S–15°N, 45°–95°E).

The east Pacific Ocean and Atlantic Ocean regions have the largest pattern correlations between surface convergence and precipitation rate, above 0.65 for every month. The east Pacific Ocean experiences two maxima in pattern correlations, March–April and September–November, and two minima, February and August–September. The Atlantic Ocean has one distinct maximum in January–February and one minimum during July–August. There is a distinct separation between the minima in pattern correlations for the Atlantic and east Pacific and the maxima in all other oceanic regions (i.e., the global tropics, the western Pacific Ocean, and the Indian Ocean). This result provides evidence that the Atlantic and east Pacific are the oceanic regions with the most robust relationship between low-level convergence and precipitation in the ITCZ.

Among the regions with lowest pattern correlations between precipitation and surface convergence, the western Pacific experiences similar month-to-month variability as the global tropics with peak correlations just above 0.6 during October–December. The Indian Ocean generally exhibits the smallest pattern correlations but it also has the largest seasonal variability. Here, pattern correlations are just above 0.55 during December–March and subside substantially during boreal summer. Both the western

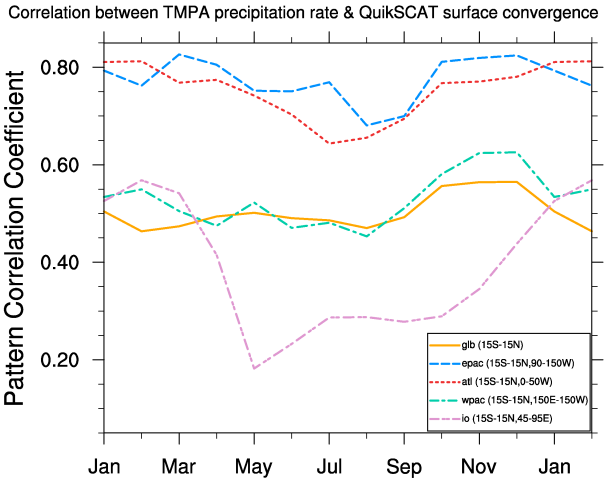

FIG. 3. Monthly pattern correlation coefficients between tropical QuikSCAT horizontal surface convergence and TMPA precipitation rate for August 1999–July 2009 for all tropical oceans (solid gold curve), the east Pacific Ocean (dashed blue curve), the Atlantic Ocean (dotted red curve), the western Pacific Ocean (dash–dotted teal curve), and the Indian Ocean (dash–dotted–dotted purple curve).

Pacific and Indian Oceans have their lowest pattern correlations during the boreal summer months, possibly due to the influence of their monsoons, which involve more zonally asymmetric precipitation features and which move poleward of our 15°S–15°N domain. Even though strong cross-equatorial pressure gradients can exist in these regions during boreal summer, common dynamical ITCZ predictors, such as low-level convergence or the zero-absolute vorticity line, are not always collocated with precipitation maxima (Webster 2020, chapter 13).

Figures 2 and 3 serve as motivation to further analyze the low-level dynamics in and near the east Pacific ITCZ during boreal spring but also bring to light the potential for similar future analyses over other regions and seasons. The Atlantic ITCZ during December–February is especially noteworthy for further investigation because these months are when Atlantic Ocean double ITCZ climate model biases are largest (Adam et al. 2018).

Before beginning our investigation of near-ITCZ dynamics and ITCZ precipitation over the east Pacific Ocean, we first highlight aspects of the east Pacific dynamics and precipitation that are central to our analyses to follow. Figure 4a–d show the annual daily climatology of equatorial QuikSCAT zonal surface winds, meridional surface winds, surface horizontal wind convergence, and TMPA precipitation rate over the east Pacific (90°–150°W). Note that the dashed gold and dotted blue curves are for the Northern Hemisphere (NH; 0°–6°N for winds, 1°–15°N precipitation and convergence) and Southern Hemisphere (SH; 6°S–0° for winds, 15°–1°S precipitation and convergence), respectively.

From these climatologies, it is evident that the east Pacific can be most generally described by one single Northern Hemisphere ITCZ with persistent southeasterly surface flow near the equator. However, there are sizeable differences in the climatologies south and north of the equator. The southerly flow is typically stronger north of the equator while the easterly flow is stronger south of the equator. There is also strong surface wind divergence south of the equator associated with the Hadley circulation. This asymmetric ITCZ structure changes substantially during boreal spring (February–April, shaded gray in Fig. 4). The equatorial surface southeasterlies diminish, causing a general decrease in near-equatorial wind speed (not shown), again with notable differences south and north of the equator. The southerlies weaken both south and north of the equator but the weakening is substantially larger north of the equator, ~4 m s^{-1} compared to ~1.5 m s^{-1} south of the equator. The easterlies weaken mainly south of the equator by ~1.5 m s^{-1}. At the same time that there is a weakening of equatorial surface winds and a trend to more symmetric dynamical conditions, the Southern Hemisphere ITCZ emerges and the Northern Hemisphere ITCZ weakens in both precipitation and surface convergence. This is what we call a "window of opportunity" for the double ITCZ over the east Pacific in observations and could help explain why climate model double ITCZ biases are largest during this season (Adam et al. 2018). This window of opportunity season is also noteworthy in that it allows for any substantial meridional wind anomalies to transport momentum, moisture, energy, etc. into either hemisphere, depending on whether there is southerly or northerly equatorial surface flow. Thus, it is key to understand that the occurrence of ITCZ shifts during boreal spring over the east Pacific may be directly related to the weakening of the climatological cross-equatorial surface flow. This weakening allows for any significant meridional wind anomalies to help produce favorable Southern or Northern Hemisphere–dominant ITCZ conditions. The equatorial meridional surface pressure gradient force exhibits the same climatological behavior as the surface meridional winds (not shown; Wang et al. 2015; Woelfle et al. 2019).

The sensitivity of the ITCZ to meridional wind variability has been shown to be strongly regulated by nonlinearities once the equatorial meridional winds reach a particular threshold magnitude (Gonzalez et al. 2016; Gonzalez and Schubert 2019). Thus, a large focus of this paper will be on the meridional wind variability in association with observed synoptic time scale ITCZ shifting and splitting. Note that most of our analyses will be focused on using ERA5 winds and divergence rather than QuikSCAT to increase sample sizes for individual ITCZ events and to quantify the horizontal momentum budgets. Note that complementary results using QuikSCAT are shown in Figs. S2–S4 in the online supplemental material.

b. *ITCZ event lagged composites*

In this section, we investigate how large-scale dynamical features change in the 6 days leading up to the two most common February–April ITCZ events, nITCZ and dITCZ. For all map plots, only statistically significant grid points at the $\alpha = 0.1$ level are shaded. Horizontal wind vectors are plotted if either the zonal or meridional component is statistically significant.

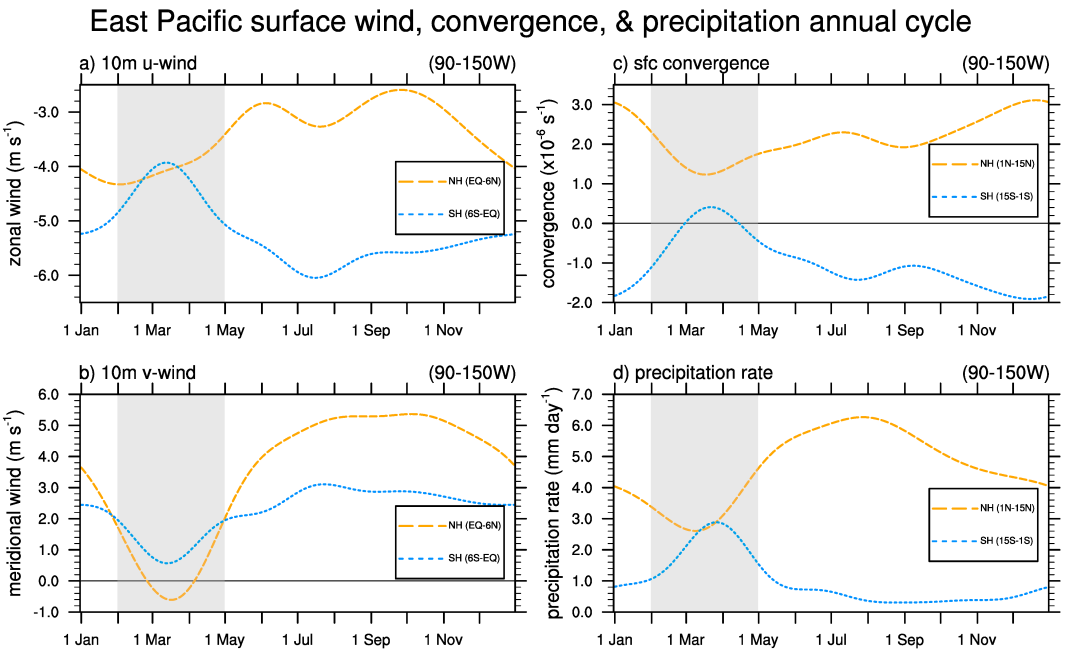

FIG. 4. Smoothed daily annual cycles of QuikSCAT surface near-equatorial (a) zonal winds, (b) meridional winds, and (c) convergence, and (d) TMPA precipitation rate averaged over the east Pacific Ocean (90°–150°W). Northern and Southern Hemisphere values are denoted by the dashed gold and dotted blue curves, respectively. The months of February–April are highlighted by the gray shading, indicating the months when double ITCZs are most prevalent.

Figures 5 and 6 show ERA5 meridional and zonal surface wind anomalies (shading) along with horizontal surface wind vectors in the days leading up to and the day of (lag −6, −3, 0 days) nITCZ and dITCZ events for February–April 1980–2012.

Preceding nITCZ events, there is a zonally elongated swath of equatorial southerly wind anomalies extending across the Pacific Ocean that intensifies with time. These southerlies speed up south of the equator and slow down north of the equator. They are therefore associated with strong meridional wind divergence and convergence bands in the Southern and Northern Hemisphere ITCZ belts, respectively (as seen in Fig. 8). There are also significant northwesterly winds in the 10°–20°S region that contribute to strong meridional divergence in the Southern Hemisphere. The east Pacific equatorial zonal surface winds illustrate the Coriolis deflection of the equatorial southerly flow, with easterlies south of the equator and westerlies north of the equator. Similar to the equatorial southerlies, the easterlies centered just south of the equator intensify leading up to nITCZ events.

The meridional wind anomalies leading up to dITCZ events are nearly the opposite of those prior to nITCZ events, with a build-up of equatorial northerlies and subtropical southerlies converging in the Southern Hemisphere ITCZ belt. The anomalous cross-equatorial northerly flow is more zonally confined for dITCZ events than it is for nITCZ events, which corresponds well with the more zonally confined anomalous precipitation and meridional convergence in Figs. 7 and 8, respectively. Similar to nITCZ events, the east Pacific equatorial zonal winds illustrate the Coriolis deflection of the equatorial northerly flow for dITCZ events, with easterlies north of the equator and westerlies centered slightly south of the equator. In the Southern Hemisphere, there is a large region of southeasterlies oriented on a southeast to northwest diagonal spanning the entire Pacific. This large-scale wind structure could be related to variations in the Pacific Walker circulation; however, this is beyond the scope of our focus on the near-surface dynamics.

Figure 7 shows the 1998–2012 TMPA precipitation rate anomalies (shading) along with 1980–2012 ERA5 horizontal surface wind vectors 6 and 3 days leading up to and the day of (lag = −6, −3, 0 days) nITCZ and dITCZ events for February–April. The nITCZ events are associated with a strengthening broad, anomalously dry region spanning the eastern to central Pacific just south of the equator and a thin and zonally elongated anomalously wet region to its north spanning nearly the entire Pacific at lag = 0. These precipitation anomalies constructively interfere with the climatological north ITCZ and destructively interfere with the climatological south ITCZ (see Fig. 2), producing one strong north ITCZ in total precipitation (not shown). The dITCZ events show less coherent statistically significant precipitation anomalies, with a thin and zonally elongated anomalously wet region in the far southeast Pacific Ocean at lag = 0 (90°–125°W) along with dry anomalies centered on the and north of the equator extending westward. While the dITCZ precipitation anomaly signals are less pronounced than they are for nITCZ events, they do constructively interfere with

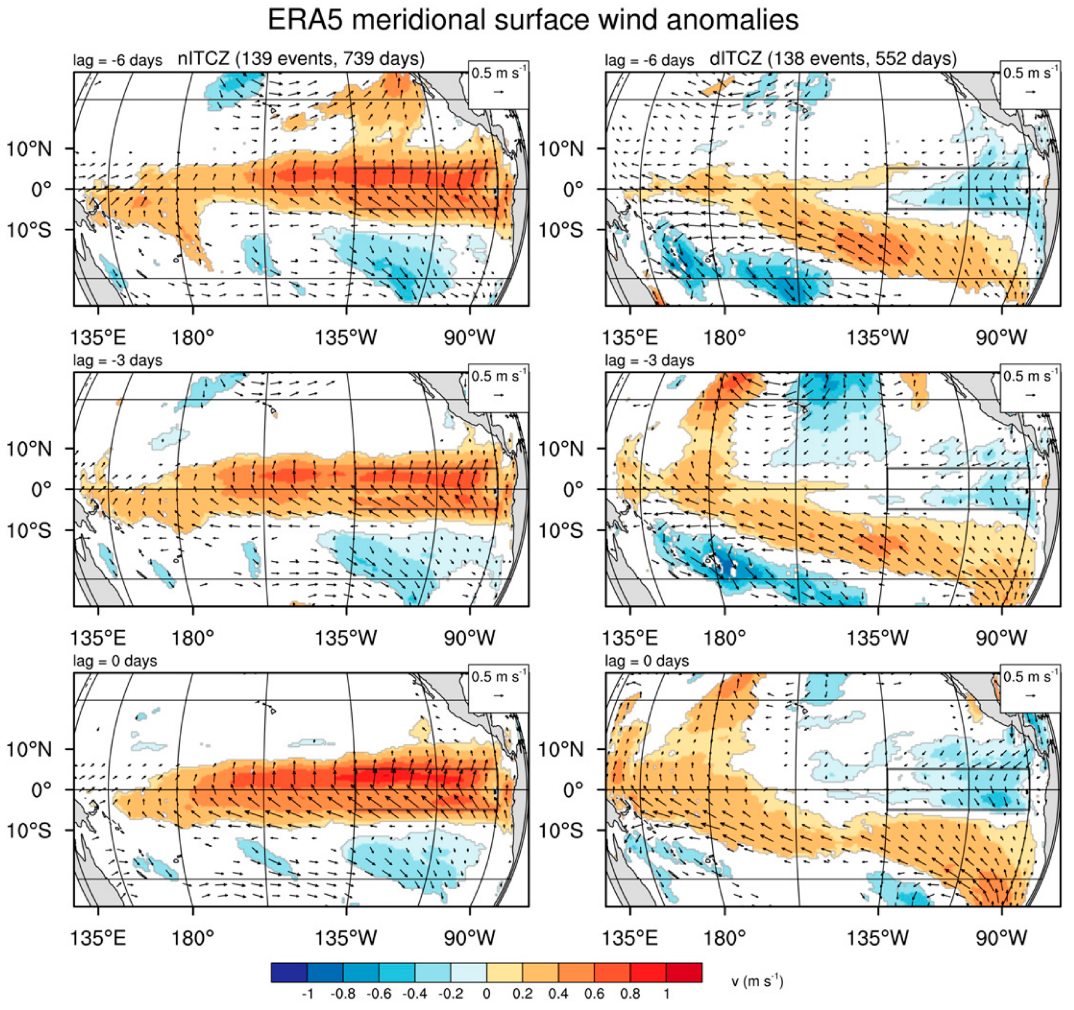

FIG. 5. Composite ERA5 meridional surface wind anomalies (shading) and horizontal surface wind anomalies (vectors) for the days preceding (lag = −6 and −3) and the day of (lag = 0) (left) nITCZ and (right) dITCZ events during February–April during 1980–2012. Only grid points where anomalies are statistically significant at the $\alpha = 0.1$ level are plotted (Wilks 2016). The gray boxed region is where the meridional winds are averaged in the middle panels of Fig. 9.

the climatological south ITCZ (see Fig. 2), making the total precipitation in the east Pacific for dITCZ events more symmetric about the equator (not shown).

In Fig. 8, we plot ERA5 meridional surface divergence anomalies (shading) along with horizontal surface wind vectors 6 and 3 days leading up to and the day of (lag = −6, −3, 0 days) nITCZ and dITCZ events for February–April 1980–2012. Similar results are obtained for the horizontal surface divergence (not shown). Similar to the TMPA precipitation rate anomalies, the meridional divergence anomalies show several narrow bands stretching across the east and central Pacific that strengthen leading up to nITCZ and dITCZ events. For nITCZ events, there is a strengthening band of meridional surface convergence in the Northern Hemisphere extending to the date line. Nearly the opposite occurs for dITCZ events, with a zonally elongated convergence band in the Southern Hemisphere intensifying prior to dITCZ events. Similar to the precipitation anomalies, the meridional convergence band is more zonally confined (90°–125°W) for dITCZ events. There are also two thin, zonally elongated divergence bands leading up to nITCZ events. The southernmost divergence band destructively interferes with the climatological southern ITCZ, in line with anomalously dry conditions in TMPA precipitation. Furthermore, there is an equatorial thin and zonally elongated divergence band in nITCZ events that appears to be associated with a speed up of southerlies just north of the equator and northerlies just south of the equator leading up to nITCZ and dITCZ events, respectively. Surface meridional convergence is an accurate predictor of nITCZ and dITCZ events, lending to our assertion of the important role of low-level dynamics in east Pacific ITCZ variability.

The lagged composite map plots show both rapid and semipersistent dynamical evolution preceding nITCZ and dITCZ events. To highlight these two time scales within the context

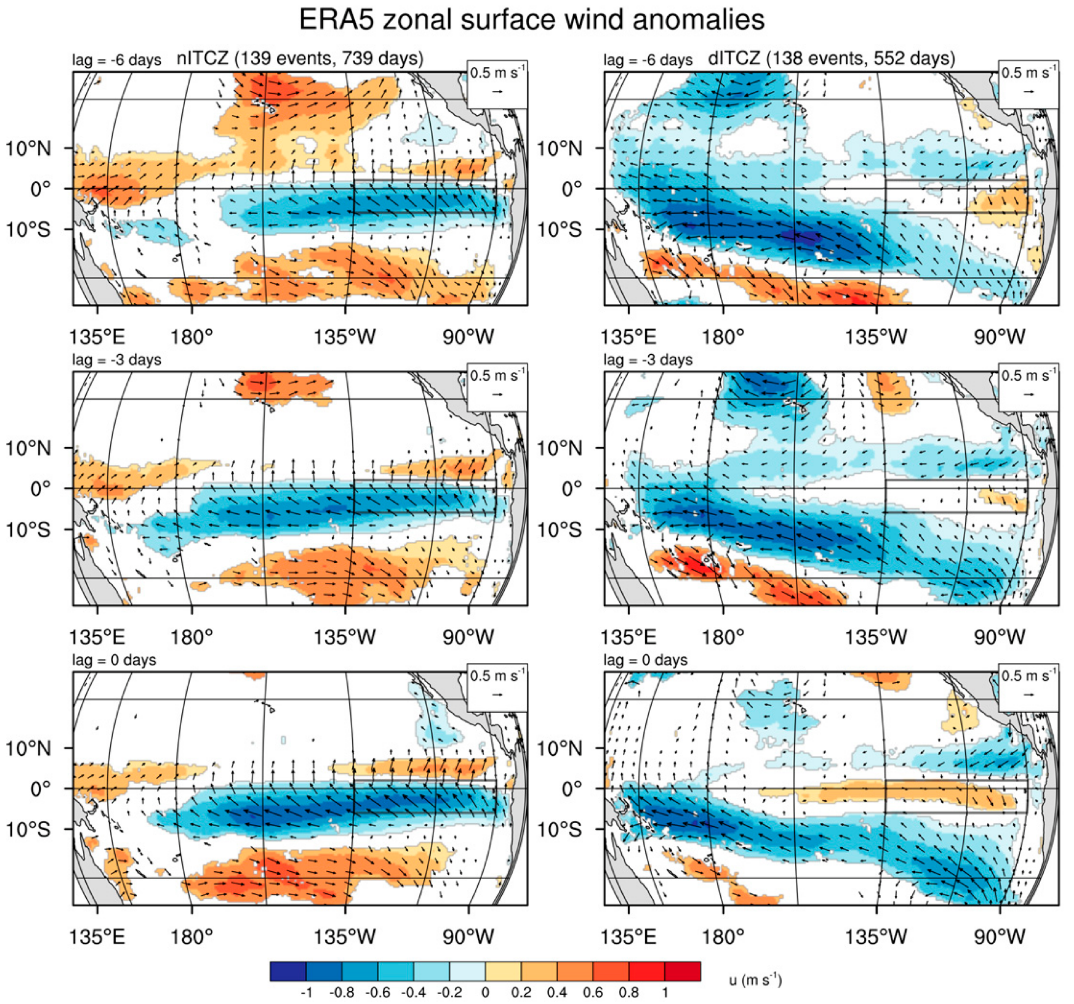

FIG. 6. As in Fig. 5, but for ERA5 zonal surface wind anomalies (shading). The gray boxed region is where the zonal winds are averaged in the bottom panels of Fig. 9.

of the time evolution of nITCZ and dITCZ dynamics, the top panels of Fig. 9 display 90°–135°W ERA5 surface convergence anomalies from 15 days before to 15 days after nITCZ and dITCZ events averaged over 4°–8°N and 8°–4°S, respectively. In the 2 weeks leading up to nITCZ events, Northern Hemisphere horizontal surface convergence anomalies intensify, with the horizontal convergence maximizing 1 day before nITCZ events. After nITCZ events, horizontal surface convergence anomalies drop off more slowly than they increased before these events. For dITCZ events, Southern Hemisphere horizontal surface convergence anomalies build up over time and peak 1 day before and the day of the beginning of dITCZ events. The decrease in horizontal surface convergence anomalies following dITCZ events occurs at a similar rate as the increase in these anomalies leading up to dITCZ events.

In the middle and bottom panel of Fig. 9, we show the 90°–135°W and 5°S–5°N meridional and 6°S–2°N zonal wind anomalies, respectively. Again, a nearly opposite dynamical evolution is seen between nITCZ and dITCZ events, with a build-up of southerly anomalies across the equator and easterly anomalies centered just south of the equator for nITCZ events, and an increase in northerly anomalies across the equator and westerly anomalies centered just south of the equator for dITCZ events. For nITCZ events, the southerlies maximize 1 day prior to, while the easterlies maximize 1 day after, these events. For dITCZ events, the same evolution is seen, with northerlies and westerlies maximizing 1 day prior to and after these events, respectively. Prominent 3–5-day oscillations also are present in the meridional surface winds, especially for dITCZ events. We hypothesize that these oscillations are related to mixed Rossby–gravity wave activity (Kiladis et al. 2016), but further investigation of these waves is outside the scope of this paper.

Due to the lack of time filtering in Fig. 9, we claim that there is a mix of daily and weekly time evolution of the near-surface dynamics that may play significant roles in driving these nITCZ and dITCZ events. In particular, we aim to understand what drives 1) the equatorial meridional flow associated with off-equatorial divergence that leads ITCZ events and 2) the equatorial/south-of-equator zonal flow that peaks after ITCZ events.

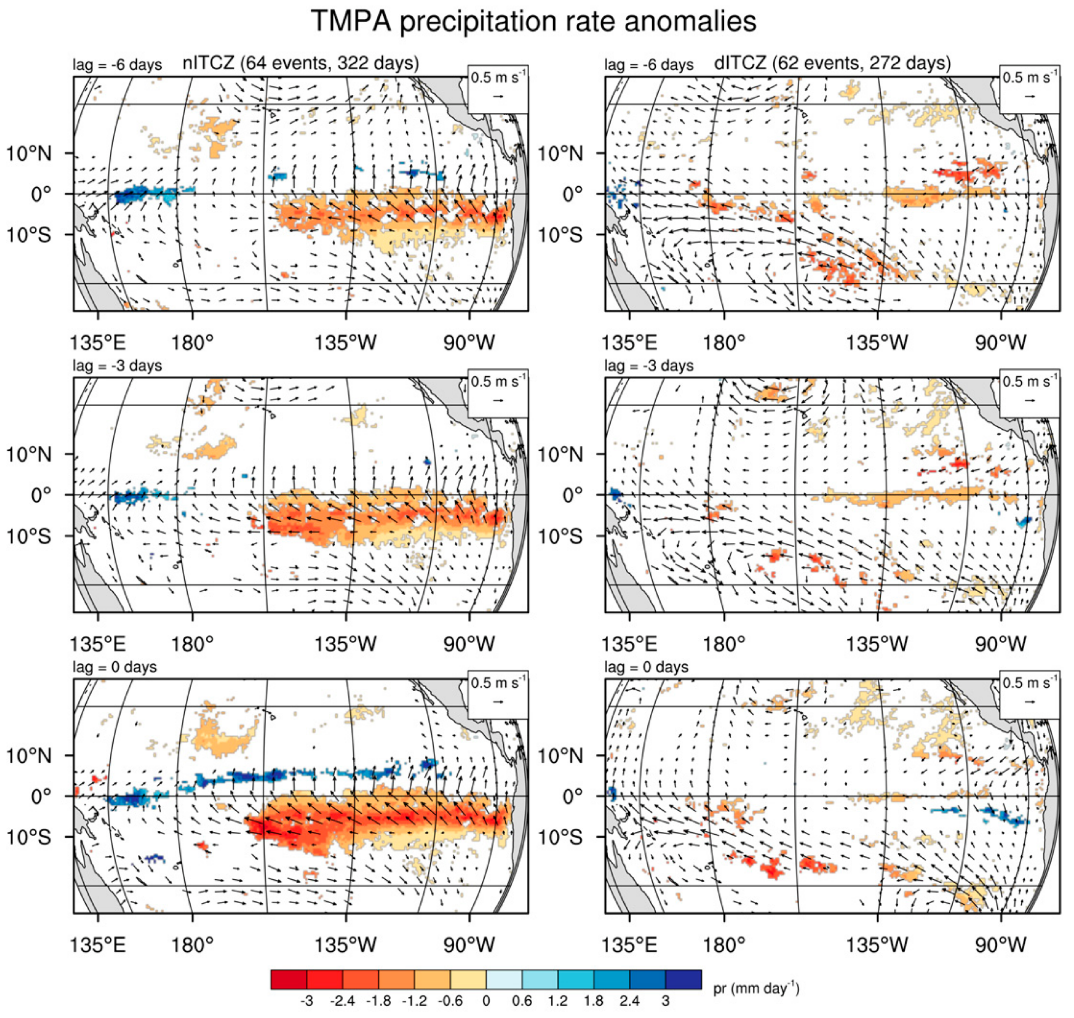

FIG. 7. As in Fig. 5 (note the inverted color map), but for 1998–2012 TMPA precipitation-rate anomalies (shading) and 1980–2012 ERA5 horizontal surface wind anomalies (vectors).

c. *Lagged zonally averaged meridional momentum budgets*

To better understand the differences in the rapidly evolving dynamics leading up to nITCZ and dITCZ events, we first examine the 90°–135°W-averaged anomalous meridional surface momentum budget 2 days preceding nITCZ and dITCZ events in Fig. 10. This lag is highlighted in orange shading in Fig. 9 and it is when the local tendency of meridional momentum, $\partial v/\partial t$, is largest. For both nITCZ and dITCZ events, the meridional momentum tendencies in the solid black curves are enhanced by a factor of 5 to highlight their signs. Note that the physical parameterizations and horizontal diffusion terms are combined, $P_v + K_v$ (thin light-purple curves), as they are the same sign and of similar magnitude (not shown).

1) nITCZ EVENTS

Preceding nITCZ events, there are sizeable southerly tendencies over 5°S–10°N, with meridional wind convergence and divergence tendencies in the 3°–10°N and 8°–3°S bands, respectively (solid black curve in Fig. 10), in broad agreement with the strengthening of the anomalous cross-equatorial flow and meridional wind convergence and divergence in Figs. 5 and 8. The leading terms in the meridional momentum budget are the pressure gradient force (PGF; dash–dotted–dotted green curve in Fig. 10) and the parameterized physics and horizontal diffusion terms (thin light-purple curve), which have southerly and northerly tendencies throughout the domain, respectively. Secondary terms in the nITCZ budget include the meridional advection of meridional momentum (dotted blue curve) and the Coriolis force (dash–dotted red curve); the zonal advection of meridional momentum (dashed orange curve) is negligible. The meridional advection of meridional momentum (dotted blue curve) produces both southerly and northerly tendencies while the Coriolis force (dash–dotted red curve) mainly produces northerly tendencies.

To gain more physical insight into the leading terms of the meridional momentum tendencies in Fig. 10, Fig. 11 shows the climatological and total (climatology + anomaly) fields used in the calculations of the anomalous meridional

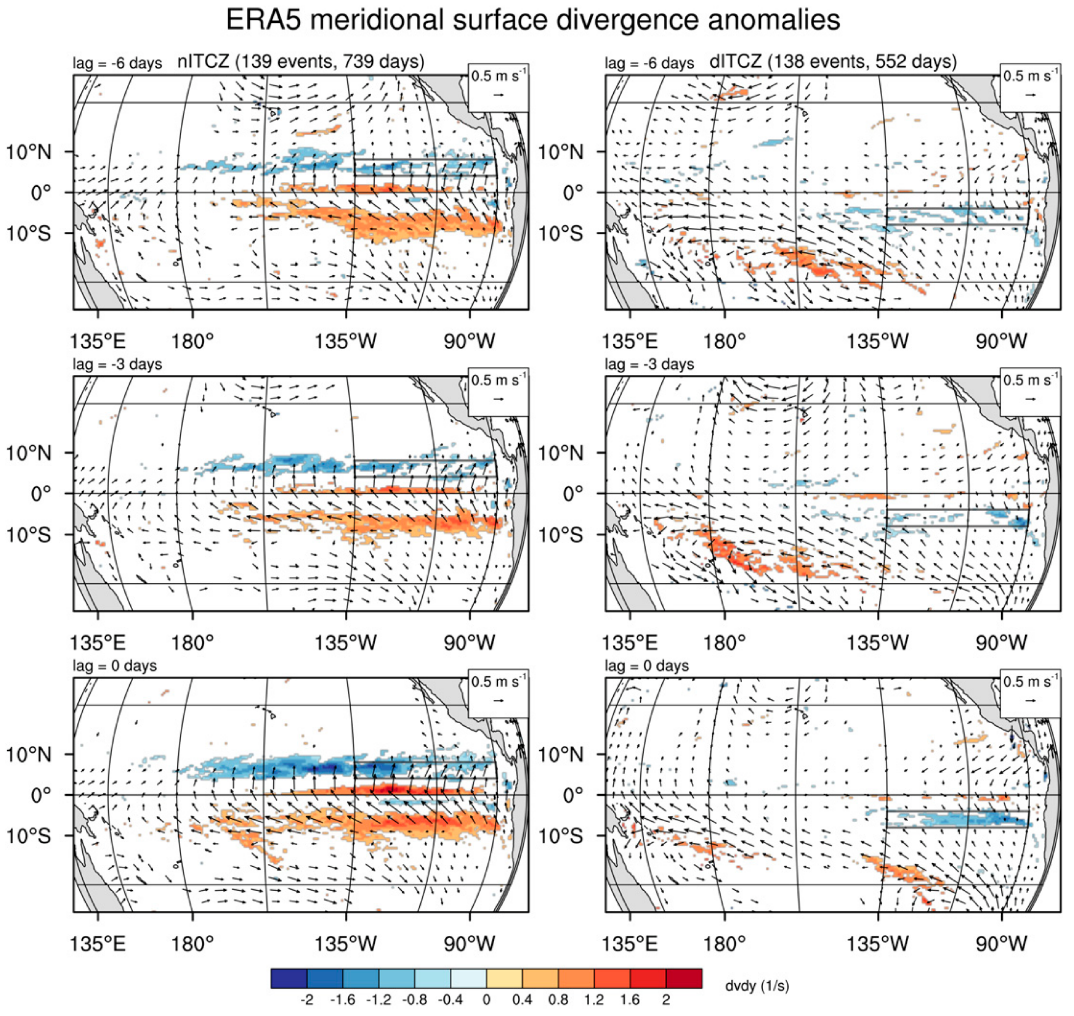

FIG. 8. As in Fig. 5, but for ERA5 meridional surface divergence anomalies (shading). The gray boxed regions are where the horizontal convergence is averaged in the top panels of Fig. 9.

momentum budget terms 2 days preceding nITCZ and dITCZ events. From the top-left to the bottom-right panels are the meridional surface (10 m) wind, zonal surface wind, surface wind speed, meridional surface wind convergence, $-\partial v/\partial y$, 2-m virtual temperature, and the meridional derivative of the natural logarithm of the mean sea level pressure, $\partial \ln p/\partial y$. Climatological fields are shown in the solid gray curves while total nITCZ and dITCZ fields are shown in the dashed blue and dotted green curves, respectively. For $\partial \ln p/\partial y$, the anomalies are plotted in the dashed blue and dotted green curves instead of the total $\partial \ln p/\partial y$. Note that the parameterized physics and horizontal diffusion terms (thin light-purple curve of Fig. 10) are broadly estimated using the $-c_D|U|v$ terms typically used in surface momentum drag parameterizations (e.g., Gonzalez et al. 2016), where c_D and $|U|$ are the surface drag coefficient and 10-m wind speed, respectively.

PGF anomalies promote southerly tendencies (dash–dotted–dotted green curve of Fig. 10), which can be primarily attributed to enhanced northerly pressure gradients, as seen in the bottom-right panel of Fig. 11. Virtual temperature anomalies have a relatively small impact on these PGF anomalies (e.g., slightly enhancing them from 2° to 0.5°S and north of 3°N; bottom-center panel of Fig. 11). On the other hand, the parameterized physics and horizontal diffusion terms (thin light-purple curve of Fig. 10) are associated with northerly tendencies that can be generally attributed to anomalously large southerlies and wind speeds south of 3°N and small northerlies and wind speeds north of 4.5°N as seen in the top-left and top-right panels of Fig. 11.

As for secondary terms in the meridional momentum nITCZ budget, the Coriolis force anomalies (dash–dotted red curve of Fig. 10), which mainly promote southerly tendencies, can be explained by anomalously large and small easterlies south of the equator and north of 2°N, respectively (top-center panel of Fig. 11). Meridional advection of the meridional momentum anomalies (dotted blue curve of Fig. 10) can primarily be attributed to anomalous meridional surface wind divergence and convergence south and

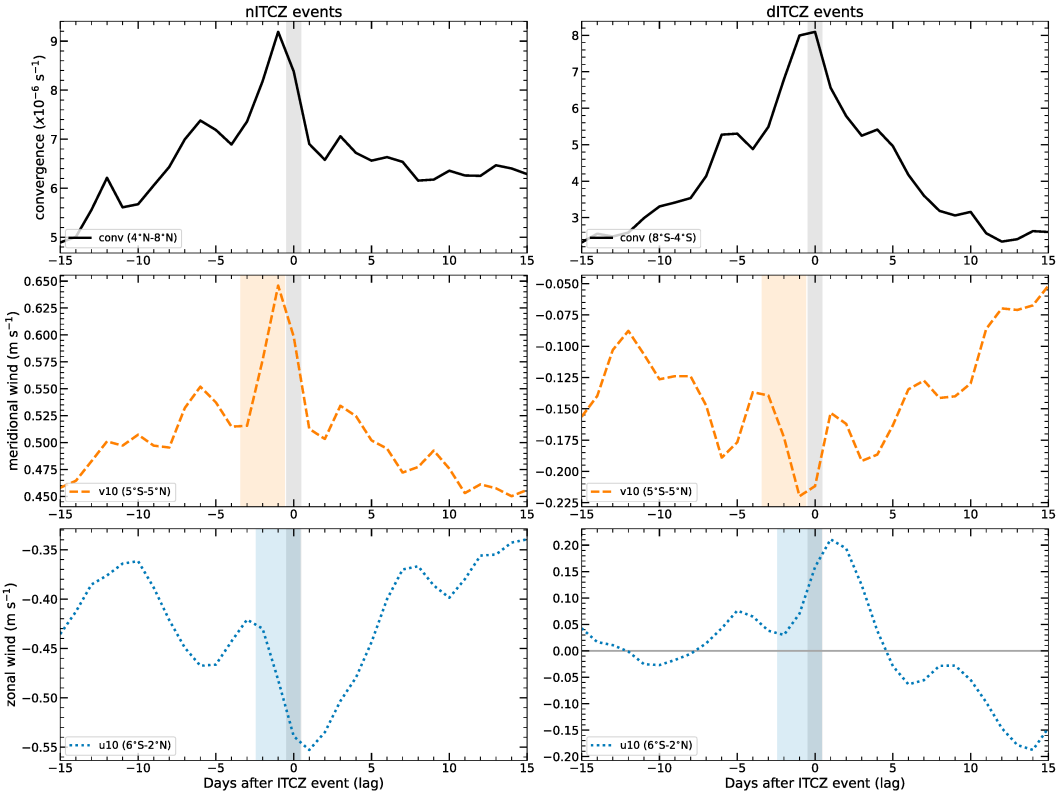

FIG. 9. Daily lag evolution composites of 90°–135°W-averaged (top) 4°–8° ERA5 horizontal surface convergence anomalies and (middle) 5°S–5°N meridional and (bottom) 6°S–2°N zonal surface wind anomalies for (left) nITCZ and (right) dITCZ events. The gray shading indicates the day of each ITCZ event while the orange and blue shading indicate the lags used in the calculation of the meridional and zonal momentum tendencies shown in the solid black curves in Figs. 10 and 12.

north of the equator, respectively, as seen in the bottom-left panel of Fig. 11.

2) dITCZ events

Returning to Fig. 10, the meridional momentum budget is generally noisier before dITCZ events than nITCZ events, especially in the 3°S–6°N region. The largest meridional momentum tendencies (solid black curve) occur over 5°S–6°N and south of 5°S, which contain northerly and southerly tendencies, respectively. The dITCZ meridional momentum tendency structure (solid black curve) acts to enhance meridional wind divergence and convergence anomalies in the 2°–7°N and 7.5°–1°S bands, respectively.

In the 5°S–6°N region, the meridional momentum budget is dominated by the PGF (dash–dotted–dotted green curve) and the parameterized physics and horizontal diffusion terms (thin light-purple curve). Similar to before nITCZ events, these two terms produce meridional tendencies of the same and opposite sign as the northerly meridional momentum tendencies (solid black curve), respectively. However, because these terms have smaller meridional momentum tendencies for dITCZ events compared to nITCZ events (note the smaller x-axis bounds), the meridional advection of meridional momentum anomalies (dotted blue curve) play a relatively more important role for dITCZ events. More specifically, the meridional advection of meridional momentum (dotted blue curve) constructively interferes with the PGF (dash–dotted–dotted green curve) and the meridional momentum tendencies (solid black curve) by producing northerly tendencies over 3.5°–0.5°S and 2.5°–6°N. The Coriolis force (dash–dotted red curve) becomes relatively large over 2.5°–6°N, producing southerly tendencies and opposing the meridional momentum tendencies (solid black curve). The zonal advection of meridional momentum (dashed orange curve) is negligible everywhere.

In the region south of 5°S, there are strong southerly tendencies (solid black curve) and all terms except the zonal advection of meridional momentum (dashed orange curve) play an important role in the anomalous meridional momentum budget. In particular, the meridional advection of meridional momentum (dotted blue curve) is key in producing strong southerly tendencies and it has a similar latitudinal structure as the meridional momentum tendencies (solid black curve) but it is shifted slightly northward. In addition to the meridional advection of meridional momentum (dotted blue curve), strong southerly tendencies over 7°–5°S are promoted by the parameterized physics and horizontal diffusion

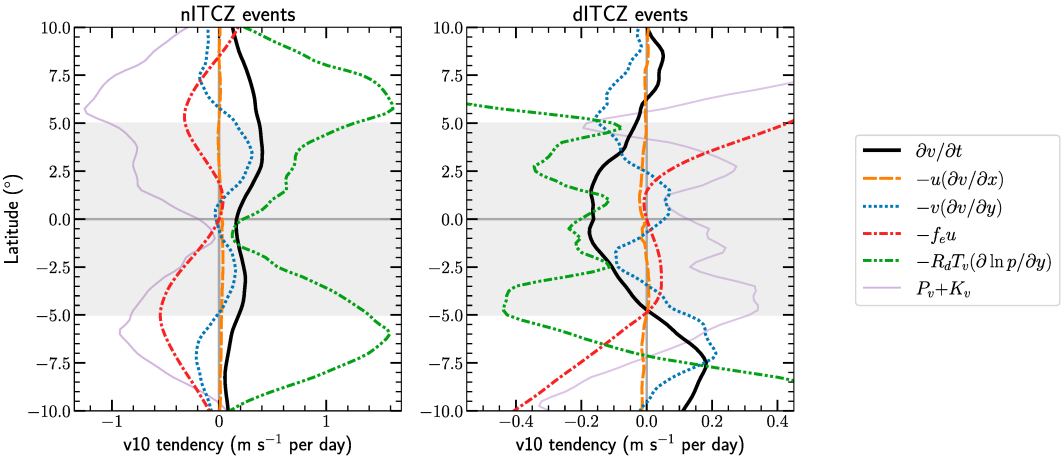

FIG. 10. Composite 90°–135°W-averaged, ERA5 meridional surface momentum budget 2 days preceding (lag = −2) (left) nITCZ and (right) dITCZ events. The gray shading indicates the meridional surface wind region used in Fig. 9. For reference, $\partial v/\partial t$ is the meridional momentum tendency, $-u(\partial v/\partial x)$ is the zonal advection of meridional momentum, $-v(\partial v/\partial y)$ is the meridional advection of meridional momentum, $-f_e u$ is the Coriolis force (including metric term), $-R_d T_v(\partial \ln p/\partial y)$ is the meridional pressure gradient force, and $P_v + K_v$ represents parameterized physical processes and horizontal diffusion.

terms (thin light-purple curve) and they are opposed by northerly tendencies associated with the Coriolis force (dash–dotted red curve) and the PGF (dash–dotted–dotted green curve). South of 7°S, the PGF (dash–dotted–dotted green curve) and the meridional advection of meridional momentum (dotted blue curve) produce strong southerly tendencies and they are opposed by the Coriolis force (dash–dotted red curve) and the parameterized physics and horizontal diffusion terms (thin light-purple curve).

Southerly and northerly tendencies driven by PGF anomalies (dash–dotted–dotted green curve of Fig. 10) can mainly be explained by anomalous southerly and northerly pressure gradients, respectively, as seen in the bottom-right panel of Fig. 11. Similar to nITCZ events, the contributions of temperature and specific humidity to meridional PGF anomalies are small; for example, anomalously warm and moist conditions slightly enhance PGF anomalies north of 3°N and from 2°S to the equator before dITCZ events (bottom-center panel of Fig. 11). Southerly tendencies associated with the parameterized physics and horizontal diffusion terms (thin light-purple curve of Fig. 10) can be attributed to anomalously weak southerlies and wind speeds from 7°S to 3.5°N, as seen in the top-left and top-right panels of Fig. 11. Furthermore, northerly tendencies associated with the parameterized physics and horizontal diffusion terms (thin light-purple curve of Fig. 10) can be explained by anomalously large northerlies and wind speeds north of 6°N and anomalously large southerlies and wind speeds south of 7°S. The northerly tendencies due to the meridional advection of meridional momentum (dotted blue curve of Fig. 10) north of 2.5°N and from 3.5° to 0.5°S can be primarily attributed to anomalous northerlies (top-left panel of Fig. 11). Southerly tendencies due to the meridional advection of meridional momentum (dotted blue curve of Fig. 10) south of 3.5°S can be explained by anomalous meridional surface wind convergence, as seen in the top-left panel of Fig. 11, associated with the anomalously strong Southern Hemisphere ITCZ associated with dITCZ events. Lastly, northerly and southerly tendencies driven by the Coriolis force (dash–dotted red curve of Fig. 10) south of 5°S and 2°N, respectively, can be attributed to anomalously strong easterlies (top-center panel of Fig. 11).

d. Lagged zonally averaged zonal momentum budgets

Figure 12 illustrates the 90°–135°W-averaged anomalous zonal surface momentum budget 1 day preceding nITCZ and dITCZ events, as this lag is when the zonal momentum tendencies are largest (blue shading in Fig. 9). Just like the meridional momentum budget in Fig. 10, the physical parameterizations and horizontal diffusion terms are combined, $P_u + K_u$ (thin light-purple curve), as they are the same sign and of similar magnitude (not shown).

1) NITCZ EVENTS

The solid black curve in Fig. 12 shows easterly tendencies south of 3°N and westerly tendencies to the north, in broad agreement with the zonal wind maps in Fig. 6. The leading terms in the nITCZ zonal momentum budget are the Coriolis force (dash–dotted red curve), pressure gradient force (PGF; dash–dotted–dotted green curve), and the parameterized physics and horizontal diffusion terms (thin light-purple curve). The Coriolis force (dash–dotted red curve) is nearly in phase with the zonal momentum tendencies (solid black curve), producing easterly and westerly tendencies south and north of the equator, respectively. The parameterized physics and horizontal diffusion terms (thin light-purple curve) nearly everywhere oppose the Coriolis force (dash–dotted red curve), producing mostly westerly and easterly tendencies south and north of the equator, respectively. Meanwhile, the PGF (dash–dotted–dotted green curve) produces easterly

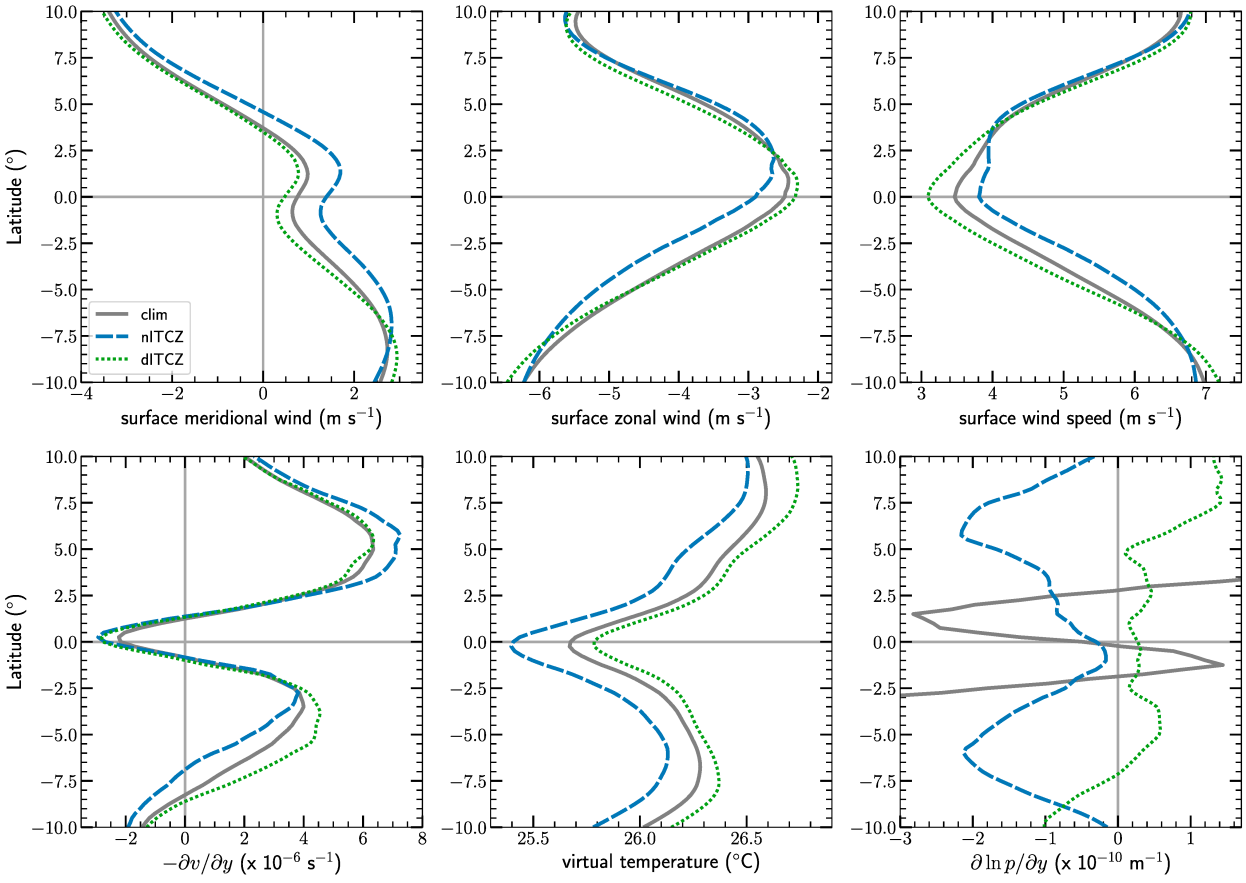

FIG. 11. Composite 90°–135°W-averaged, ERA5 climatological (solid gray curves) and total (climatology + anomaly) dynamic and thermodynamic fields 2 days preceding (lag = −2) nITCZ (dashed blue curves) and dITCZ events (dotted green curves), including (top left) meridional surface wind, (top center) zonal surface wind, (top right) surface wind speed, (bottom left) $-\partial v/\partial y$, (bottom center) 2-m virtual temperature, and (bottom right) $\partial \ln p/\partial y$, where p is the mean sea level pressure. Note that $\partial \ln p/\partial y$ anomalies are plotted as dashed blue and dotted green curves.

tendencies in the entire region. Similar to the nITCZ meridional momentum budget, the zonal advective term (dashed orange curve) is negligible and the meridional advective term (dotted blue curve) plays a secondary role in the zonal momentum budget, with both easterly and westerly tendencies.

Figure 13 shows the climatological and total (climatology + anomaly) fields used in the calculations of the anomalous zonal momentum budget terms 1 day preceding nITCZ and dITCZ events. From the top-left to the bottom-right panel are the meridional surface (10 m) wind, zonal surface wind, surface wind speed, negative meridional gradient of the zonal wind, $-\partial u/\partial y$, 2-m virtual temperature, and the zonal derivative of the natural logarithm of the mean sea level pressure, $\partial \ln p/\partial x$. Climatological fields are shown in the solid gray curves while total nITCZ and dITCZ fields are shown in the dashed blue and dotted green curves, respectively. Note that the parameterized physics and horizontal diffusion terms (thin light-purple curve of Fig. 12) are diagnosed via $-c_D|U|u$ (Gonzalez et al. 2016).

Easterly and westerly tendencies to the south and north, respectively, are dominated by the Coriolis force (dash–dotted red curve of Fig. 12); this behavior can be explained by the anomalous southerlies deflecting the flow more westward over 0°–8.5°S and more eastward in the Northern Hemisphere than usual, as seen in the top-left panel of Fig. 13. The westerly tendencies over 9°S–2°N produced by the parameterized physics and horizontal diffusion terms (thin light-purple curve of Fig. 12) can be attributed to anomalously strong easterlies and wind speeds (top-center and top-right panels of Fig. 13). At the same time, the easterly tendencies over 2°–7.5°N produced by the parameterized physics and horizontal diffusion terms (thin light-purple curve of Fig. 12) can be attributed to anomalously weak easterlies and wind speeds. Easterly PGF anomalies (dash–dotted–dotted green curve of Fig. 10) can be mainly attributed to westerly pressure gradient anomalies, with cool and dry anomalies slightly diminishing and enhancing the PGF anomalies south and north of 5°N, respectively, as seen in the bottom-center and -right panels of Fig. 13. Although a secondary term in the zonal momentum budget, the easterly and westerly tendencies associated with the meridional advection of zonal momentum (dotted blue curve of Fig. 12) over 5°S–0.5° and 0.5°–7°N, respectively, can be explained by

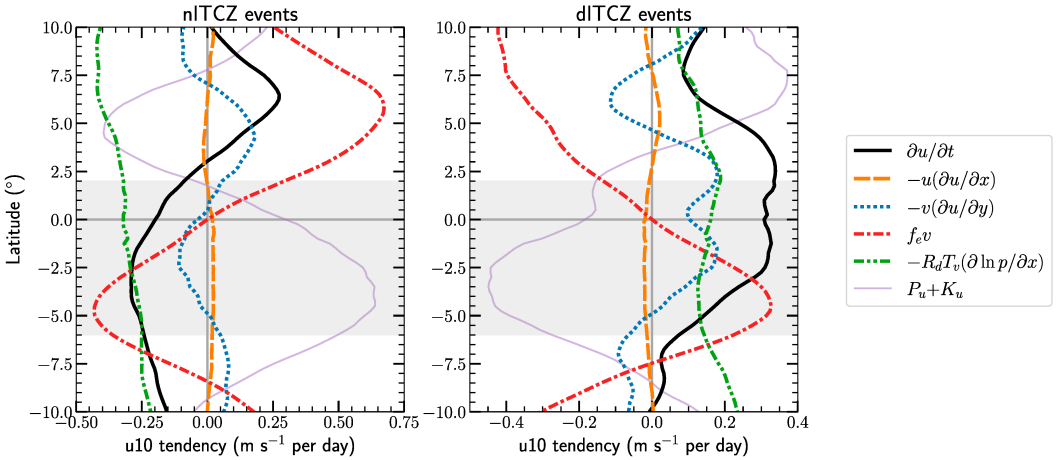

FIG. 12. As in Fig. 10, but for the zonal surface momentum budget 1 day preceding (lag = −1) (left) nITCZ and (right) dITCZ events. The gray shading indicates the zonal surface wind region used in Fig. 9. For reference, $\partial u/\partial t$ is the zonal momentum tendency, $-u(\partial u/\partial x)$ is the zonal advection of zonal momentum, $-v(\partial u/\partial y)$ is the meridional advection of zonal momentum, $f_e v$ is the Coriolis acceleration (including metric term), $-R_d T_v(\partial \ln p/\partial x)$ is the zonal pressure gradient force, and $P_u + K_u$ is the zonal momentum tendency due to parameterized physical processes and horizontal diffusion.

stronger southerlies than usual, as seen in the top and bottom-left panels of Fig. 12.

2) dITCZ EVENTS

Coming back to Fig. 12 for dITCZ events, we see westerly zonal momentum tendencies (solid black curve) in the entire domain, with a peak in westerly tendencies over the 3°S–4°N band. All terms except the zonal advection of meridional momentum (dashed orange curve) play an important role in the anomalous zonal momentum budget for dITCZ events. From 5°S to the equator, westerly tendencies are produced by the Coriolis force (dash–dotted–dotted red curve), PGF (dash–dotted–dotted green curve), and the meridional advection of zonal momentum (dotted blue curve); easterly tendencies are produced by the parameterized physics and horizontal diffusion terms (thin light-purple curve). From the equator to 3.5°N, westerly tendencies are produced by the PGF (dash–dotted–dotted green curve) and the meridional advection of zonal momentum (dotted blue curve) while easterly tendencies are produced by the parameterized physics and horizontal diffusion terms (thin light-purple curve) and the Coriolis force (dash–dotted red curve).

The westerly and easterly tendencies south and north of the equator due to the Coriolis force (dash–dotted red curve in Fig. 12) can be attributed to the northerly anomalies shown in the top-left panel of Fig. 13. The westerly tendencies produced by the PGF can be explained by anomalous easterly pressure gradients, as seen in the dashed blue curve in the bottom-right panel of Fig. 13. Anomalously warm and moist conditions slightly enhance and diminish the PGF anomalies north and south of 2.5°N, respectively (bottom-center panel of Fig. 13). The meridional advection of zonal momentum has its largest impact producing westerly tendencies over 5°S–4.5°N, which can be explained by anomalously weak southerlies over 5°S–0.5°N and anomalously strong meridional gradients of the zonal wind from 0.5°–4.5°N, as seen in the top and bottom-left panels of Fig. 13. The easterly and westerly tendencies produced by the parameterized physics and horizontal diffusion terms (thin light-purple curve of Fig. 12) are attributed to anomalously weak easterlies and wind speeds from 7°S–3°N and anomalously strong easterlies and wind speeds north of 4°N, respectively.

4. Summary and conclusions

February–April is a unique season over the tropical east Pacific Ocean when it has been observed that the ITCZ experiences daily–weekly latitudinal shifts and splits (Haffke et al. 2016). Using QuikSCAT surface winds and TMPA precipitation, we show that the east Pacific and Atlantic Oceans are the regions where the large-scale, zonally elongated bands of tropical surface convergence and precipitation are most strongly correlated on monthly time scales, which motivates the usefulness of investigating transient, near-surface ITCZ dynamics over the east Pacific. We demonstrate that February–April is a climatological "window of opportunity" for the emergence of double ITCZs and strong variability in ITCZ position over the east Pacific; as the near-equatorial surface (especially meridional) winds decay, the Northern Hemisphere ITCZ weakens and the Southern Hemisphere ITCZ strengthens so that both ITCZs get closer to near-equal strength. Furthermore, any significant equatorial meridional wind variability about the climatological mean has the potential to substantially alter the interhemispheric transport of temperature, moisture, energy, momentum, and thus, the latitudinal location of the zonally elongated convergence bands.

We utilize subdaily ITCZ states from a pattern recognition algorithm (Henke et al. 2012; Haffke et al. 2016) to illustrate

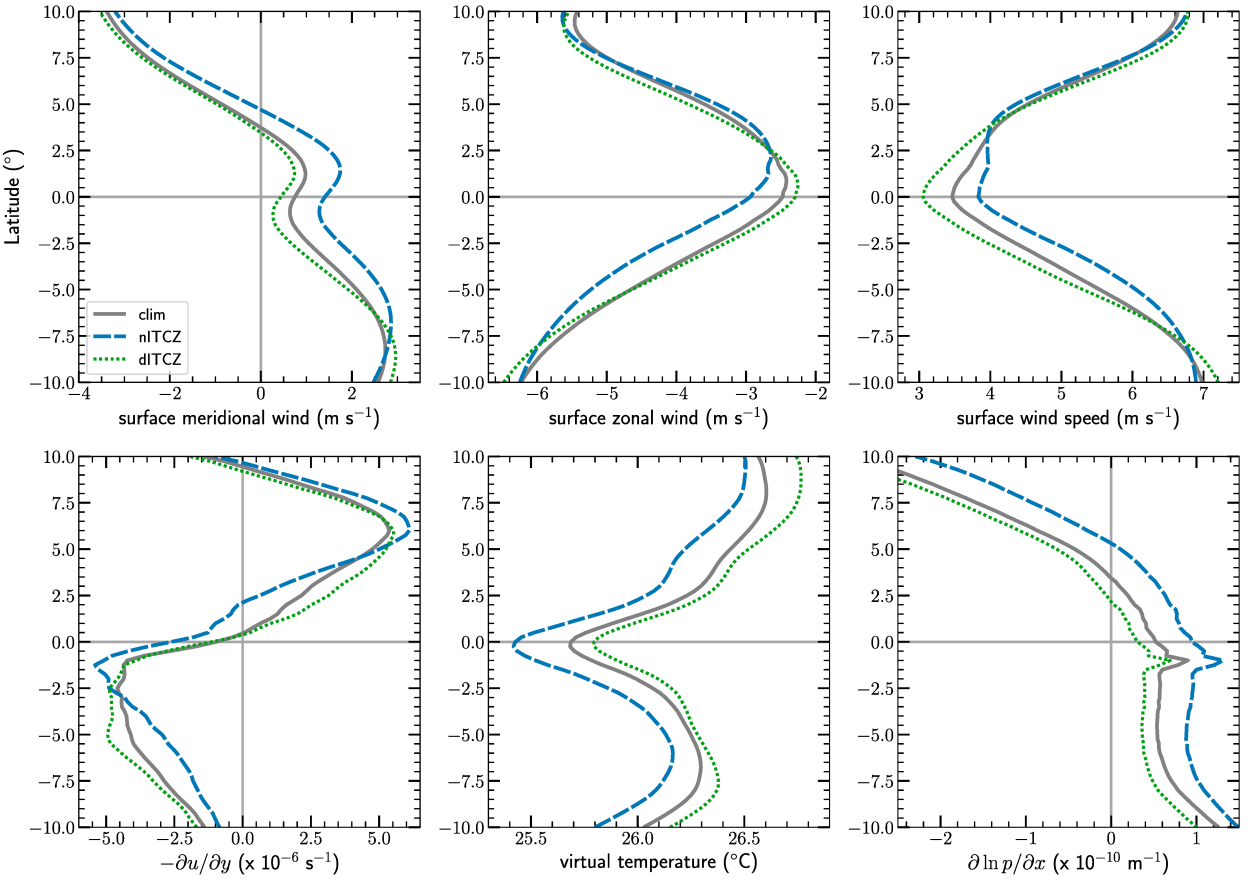

FIG. 13. As in Fig. 11, but 1 day before (lag = −1) nITCZ and dITCZ events. Note that $-\partial u/\partial y$, not $-\partial v/\partial y$, is in the bottom-left panel and the total field of $\partial \ln p/\partial y$ before nITCZ and dITCZ events are plotted as the dashed blue and dotted green curves, respectively.

the time evolution of the large-scale near-surface dynamics in ERA5 associated with the two most common February through April submonthly (2–30 days) ITCZ events, northern (nITCZ) and double ITCZ (dITCZ) events. There is a rapid (daily) and slower (weekly) anomalous dynamical evolution associated with both nITCZ and dITCZ events. One to two days prior to nITCZ events, there is a peak in cross-equatorial southerly and northwesterly Southern Hemisphere subtropical anomalous flows that stretch across the east and central Pacific. The southerly tendencies are in phase with intensifying zonally elongated anomalous divergence and convergence bands in the Southern and Northern Hemispheres, respectively. One or two days later, an elongated band of easterly anomalies centered just south of the equator maximizes. There is a similar intensification of cross-equatorial northerly and Southern Hemisphere convergence anomalies that peak 1 day prior to or the day of dITCZ events, but they are more zonally confined to the east Pacific. South of the Southern Hemisphere convergence band, there is a zonally elongated region of strong southeasterly anomalies leading up to dITCZ events that is associated with an anomalously strong subtropical high and may contribute to Southern Hemisphere ITCZ intensification. One or two days after the peak in equatorial northerly and Southern Hemisphere convergence anomalies, zonally elongated westerly anomalies appear centered just south of the equator. Thus, we see a rapid evolution of meridional winds and off-equatorial convergence and divergence bands peaking 1 or 2 days before nITCZ and dITCZ events followed by a peak in zonal winds 1 or 2 days later.

Although beyond the scope of this study, we note that the anomalous near-equatorial southeasterlies that intensify during nITCZ events constructively interfere with the background flow, enhancing surface wind speeds, the east Pacific equatorial cold tongue, and meridional surface pressure gradients on and north of the equator (i.e., Fig. 11). On the other hand, dITCZ events are associated with diminished surface wind speeds, a weaker equatorial cold tongue, and enhanced meridional surface pressure gradients south of the equator (i.e., Fig. 11). How these opposing behaviors of nITCZ and dITCZ events fit into wind–evaporation–SST feedback theory (Xie and Philander 1994) and other mechanisms will be explored in a follow-up study.

To improve our understanding of the physical mechanisms driving the time evolution of the near-surface zonal and meridional wind anomalies over the east Pacific, we quantify the zonally averaged anomalous zonal and meridional momentum budgets when the zonal and meridional momentum tendencies peak, 1 and 2 days prior to nITCZ and dITCZ events, respectively. The zonal and meridional

momentum budgets before nITCZ events show important roles for the pressure gradient force (PGF), Coriolis force, and the parameterized physics and horizontal diffusion terms, which we mainly attribute to surface momentum drag (Gonzalez et al. 2016). Therefore, the anomalous first-order, low-level dynamics associated nITCZ events appear to be driven by the three terms in Ekman balance. More specifically, southerly cross-equatorial flow is promoted by the meridional PGF while near-equatorial easterlies are driven by the zonal PGF and the Coriolis force preceding nITCZ events. Secondary contributions to the nITCZ anomalous momentum budgets come from meridional advection of the horizontal momentum. On the contrary, the meridional advection of horizontal momentum terms play just as an important of a role as the PGF, Coriolis force, and the parameterized physics and horizontal diffusion terms before dITCZ events due in part to the smaller accelerations produced by latter three terms. More specifically, northerly cross-equatorial flow is promoted by the meridional PGF and the meridional advection of meridional wind while near-equatorial westerly tendencies are driven by the meridional advection of zonal momentum, the zonal PGF, and the Coriolis force. Last, southerly tendencies south of 5°S that "feed" into the southern ITCZ are highly correlated with meridional advection of meridional momentum anomalies.

Comparing the climatological and total (climatology + anomaly) dynamic and thermodynamic fields before dITCZ and nITCZ events demonstrates that horizontal PGF anomalies can be primarily attributed to variations in pressure gradients and less so to variations in temperature or specific humidity. We also observe weaker equatorial wind speeds and more symmetric dynamical (horizontal winds and convergence) latitudinal structure associated with the westerly and northerly anomalies before dITCZ events, and the opposite for nITCZ events (see Figs. 11 and 13). The equatorial westerly tendencies and anomalously weak east Pacific cold tongue prior to dITCZ events are consistent with the anti-Hadley circulation negative feedback mechanism discussed in Adam (2021), wherein geostrophically balanced westerlies balance the easterly ocean wind stress that promotes equatorial upwelling. Furthermore, our zonal momentum budget for dITCZ events south of the equator is qualitatively consistent with the symmetric anti-Hadley circulation associated with Fig. 7 of Adam (2021), in that there is an anomalous poleward flow that dominates the meridional advection of the zonal momentum.

While the meridional advective terms are often smaller than the Coriolis and pressure gradient forces, they are much less variable on a day-to-day basis (shown in Figs. S5 and S6 in the online supplemental material), implying that they play a primary role in driving zonal and meridional momentum tendencies for some nITCZ and dITCZ events. Thus, it comes as no surprise that models struggle to simulate the ITCZ surrounding the months of February through April (Adam et al. 2018) as small errors in any one of the momentum budget terms could lead to errors in ITCZ dynamics in model simulations. Improving our understanding of subseasonal nITCZ and dITCZ events in observations and reanalyses is a step in the right direction to formulating a more complete theory of oceanic ITCZs. While this study has placed focus on the east Pacific Ocean ITCZ, our analyses could be extended to the Atlantic Ocean ITCZ, which also experiences substantial climate model biases (Adam et al. 2018). The Atlantic, similar to the east Pacific, exhibits strong correlations between tropical surface convergence and precipitation (e.g., Fig. 3).

Acknowledgments. We thank Gudrun Magnusdottir, Spencer Hill, Juan Lora, Anantha Aiyyer, and Bill Gutowski for fruitful discussions that helped us in developing ideas for this manuscript. We also would like to thank two anonymous reviewers. Financial support comes from NSF Grant AGS-1953944 and startup funding from Iowa State University.

Data availability statement. The QuikSCAT data can be downloaded from https://podaac.jpl.nasa.gov/dataset/QSCAT_LEVEL_3_V2. The TMPA data can be downloaded from https://disc.gsfc.nasa.gov/datasets/TRMM_3B42_Daily_7/summary. The ERA5 surface data can be downloaded from https://cds.climate.copernicus.eu/cdsapp#!/dataset/reanalysis-era5-single-levels?tab=overview. All scripts used to produce figures for this paper are located online via the repository at https://iastate.box.com/v/itczshifts-obstheory.

REFERENCES

Adam, O., 2021: Dynamic and energetic constraints on the modality and position of the intertropical convergence zone in an aquaplanet. *J. Climate*, **34**, 527–543, https://doi.org/10.1175/JCLI-D-20-0128.1.

——, T. Schneider, and F. Brient, 2018: Regional and seasonal variations of the double-ITCZ bias in CMIP5 models. *Climate Dyn.*, **51**, 101–117, https://doi.org/10.1007/s00382-017-3909-1.

Back, L. E., and C. S. Bretherton, 2009: On the relationship between SST gradients, boundary layer winds, and convergence over the tropical oceans. *J. Climate*, **22**, 4182–4196, https://doi.org/10.1175/2009JCLI2392.1.

Bellucci, A., S. Gualdi, and A. Navarra, 2010: The double-ITCZ syndrome in coupled general circulation models: The role of large-scale vertical circulation regimes. *J. Climate*, **23**, 1127–1145, https://doi.org/10.1175/2009JCLI3002.1.

Burgers, J. M., 1948: A mathematical model illustrating the theory of turbulence. *Adv. Appl. Mech.*, **1**, 171–199, https://doi.org/10.1016/S0065-2156(08)70100-5.

Duffy, M. L., P. A. O'Gorman, and L. E. Back, 2020: Importance of Laplacian of low-level warming for the response of precipitation to climate change over tropical oceans. *J. Climate*, **33**, 4403–4417, https://doi.org/10.1175/JCLI-D-19-0365.1.

Ekman, V. W., 1905: On the influence of the Earth's rotation on ocean currents. *Ark. Mat. Astron. Fys.*, **2** (11), 1–52.

Gonzalez, A. O., and W. H. Schubert, 2019: Violation of Ekman balance in the eastern Pacific ITCZ boundary layer. *J. Atmos. Sci.*, **76**, 2919–2940, https://doi.org/10.1175/JAS-D-18-0291.1.

——, C. J. Slocum, R. K. Taft, and W. H. Schubert, 2016: Dynamics of the ITCZ boundary layer. *J. Atmos. Sci.*, **73**, 1577–1592, https://doi.org/10.1175/JAS-D-15-0298.1.

Haffke, C., G. Magnusdottir, D. Henke, P. Smyth, and Y. Peings, 2016: Daily states of the March–April east Pacific ITCZ in three decades of high-resolution satellite data. *J. Climate*, **29**, 2981–2995, https://doi.org/10.1175/JCLI-D-15-0224.1.

Henke, D., P. Smyth, C. Haffke, and G. Magnusdottir, 2012: Automated analysis of the temporal behavior of the double intertropical convergence zone over the east Pacific. *Remote Sens. Environ.*, **123**, 418–433, https://doi.org/10.1016/j.rse.2012.03.022.

Hersbach, H., and Coauthors, 2020: The ERA5 global reanalysis. *Quart. J. Roy. Meteor. Soc.*, **146**, 1999–2049, https://doi.org/10.1002/qj.3803.

Hill, S. A., 2019: Theories for past and future monsoon rainfall changes. *Curr. Climate Change Rep.*, **5**, 160–171, https://doi.org/10.1007/s40641-019-00137-8.

Holton, J. R., 1975: On the influence of boundary layer friction on mixed Rossby-gravity waves. *Tellus*, **27**, 107–115, https://doi.org/10.3402/tellusa.v27i2.9893.

Huffman, G. J., and D. T. Bolvin, 2015: TRMM and other data precipitation data set documentation. NASA Goddard Space Flight Center, 44 pp., https://pmm.nasa.gov/sites/default/files/document_files/3B42_3B43_doc_V7.pdf.

Kang, S. M., Y. Shin, and S.-P. Xie, 2018: Extratropical forcing and tropical rainfall distribution: Energetics framework and ocean Ekman advection. *npj Climate Atmos. Sci.*, **1**, 20172, https://doi.org/10.1038/s41612-017-0004-6.

Kiladis, G. N., J. Dias, and M. Gehne, 2016: The relationship between equatorial mixed Rossby–gravity and eastward inertio-gravity waves. Part I. *J. Atmos. Sci.*, **73**, 2123–2145, https://doi.org/10.1175/JAS-D-15-0230.1.

Knapp, K. R., and Coauthors, 2011: Globally gridded satellite observations for climate studies. *Bull. Amer. Meteor. Soc.*, **92**, 893–907, https://doi.org/10.1175/2011BAMS3039.1.

Lin, J.-L., 2007: The double-ITCZ problem in IPCC AR4 coupled GCMs: Ocean–atmosphere feedback analysis. *J. Climate*, **20**, 4497–4525, https://doi.org/10.1175/JCLI4272.1.

Lindzen, R. S., and S. Nigam, 1987: On the role of sea surface temperature gradients in forcing low-level winds and convergence in the tropics. *J. Atmos. Sci.*, **44**, 2418–2436, https://doi.org/10.1175/1520-0469(1987)044<2418:OTROSS>2.0.CO;2.

Liu, W. T., and X. Xie, 2002: Double intertropical convergence zones—A new look using scatterometer. *Geophys. Res. Lett.*, **29**, 2072, https://doi.org/10.1029/2002GL015431.

Mahrt, L. J., 1972: A numerical study of the influence of advective accelerations in an idealized, low-latitude, planetary boundary layer. *J. Atmos. Sci.*, **29**, 1477–1484, https://doi.org/10.1175/1520-0469(1972)029<1477:ANSOTI>2.0.CO;2.

McGauley, M., C. Zhang, and N. Bond, 2004: Large-scale characteristics of the atmospheric boundary layer in the eastern Pacific cold tongue-ITCZ region. *J. Climate*, **17**, 3907–3920, https://doi.org/10.1175/1520-0442(2004)017<3907:LCOTAB>2.0.CO;2.

Mechoso, C., and Coauthors, 1995: The seasonal cycle over the tropical Pacific in coupled ocean–atmosphere general circulation models. *Mon. Wea. Rev.*, **123**, 2825–2838, https://doi.org/10.1175/1520-0493(1995)123<2825:TSCOTT>2.0.CO;2.

Schneider, T., and S. Bordoni, 2008: Eddy-mediated regime transitions in the seasonal cycle of a Hadley circulation and implications for monsoon dynamics. *J. Atmos. Sci.*, **65**, 915–934, https://doi.org/10.1175/2007JAS2415.1.

——, T. Bischoff, and G. H. Haug, 2014: Migrations and dynamics of the intertropical convergence zone. *Nature*, **513**, 45–53, https://doi.org/10.1038/nature13636.

SeaPAC, 2006: Seawinds on QuikSCAT level 3 daily gridded ocean wind vectors (JPL version 2). NASA PO.DAAC, accessed 25 October 2018, https://doi.org/10.5067/QSXXX-L3002.

Sobel, A. H., and J. D. Neelin, 2006: The boundary layer contribution to intertropical convergence zones in the quasi-equilibrium tropical circulation model framework. *Theor. Comput. Fluid Dyn.*, **20**, 323–350, https://doi.org/10.1007/s00162-006-0033-y.

Song, X., and G. J. Zhang, 2019: Culprit of the eastern Pacific double-ITCZ bias in the NCAR CESM1.2. *J. Climate*, **32**, 6349–6364, https://doi.org/10.1175/JCLI-D-18-0580.1.

Stevens, B., J. Duan, J. C. McWilliams, M. Münnich, and J. D. Neelin, 2002: Entrainment, Rayleigh friction, and boundary layer winds over the tropical Pacific. *J. Climate*, **15**, 30–44, https://doi.org/10.1175/1520-0442(2002)015<0030:ERFABL>2.0.CO;2.

Tian, B., and X. Dong, 2020: The double-ITCZ bias in CMIP3, CMIP5, and CMIP6 models based on annual mean precipitation. *Geophys. Res. Lett.*, **47**, e2020GL087232, https://doi.org/10.1029/2020GL087232.

Tomas, R. A., J. R. Holton, and P. J. Webster, 1999: The influence of cross-equatorial pressure gradients on the location of near-equatorial convection. *Quart. J. Roy. Meteor. Soc.*, **125**, 1107–1127, https://doi.org/10.1002/qj.1999.49712555603.

Wang, C.-C., W.-L. Lee, Y.-L. Chen, and H.-H. Hsu, 2015: Processes leading to double intertropical convergence zone bias in CESM1/CAM5. *J. Climate*, **28**, 2900–2915, https://doi.org/10.1175/JCLI-D-14-00622.1.

Webster, P. J., 2020: Dynamics of the tropical atmosphere and oceans. *Texts in Applied Mathematics.* 1st ed. Wiley-Blackwell, 536 pp.

Wilks, D. S., 2016: "The stippling shows statistically significant grid points": How research results are routinely overstated and overinterpreted, and what to do about it. *Bull. Amer. Meteor. Soc.*, **97**, 2263–2273, https://doi.org/10.1175/BAMS-D-15-00267.1.

Woelfle, M. D., C. S. Bretherton, C. Hannay, and R. Neale, 2019: Evolution of the double-ITCZ bias through CESM2 development. *J. Adv. Model. Earth Syst.*, **11**, 1873–1893, https://doi.org/10.1029/2019MS001647.

Xie, S.-P., and S. G. H. Philander, 1994: A coupled ocean–atmosphere model of relevance to the ITCZ in the eastern Pacific. *Tellus*, **46**, 340–350, https://doi.org/10.3402/tellusa.v46i4.15484.

Yang, W., and G. Magnusdottir, 2016: Interannual signature in daily ITCZ states in the east Pacific in boreal spring. *J. Climate*, **29**, 8013–8025, https://doi.org/10.1175/JCLI-D-16-0395.1.

Zhang, X., L. Hailong, and Z. Minghua, 2015: Double ITCZ in coupled ocean–atmosphere models: From CMIP3 to CMIP5. *Geophys. Res. Lett.*, **42**, 8651–8659, https://doi.org/10.1002/2015GL065973.